



Detection of biomolecules and bioconjugates by monitoring rotated grating-coupled surface plasmon resonance

EMESE TÓTH,¹ ANIKÓ SZALAI,¹ ANIKÓ SOMOGYI,¹ BALÁZS BÁNHÉLYI,²
EDIT CSAPÓ,^{3,4} IMRE DÉKÁNY,³ TIBOR CSENDES,² AND MÁRIA CSETE^{1,*}

¹Department of Optics and Quantum Electronics, University of Szeged, H-6720, Dóm tér 9, Szeged, Hungary

²Institute of Informatics, University of Szeged, H-6720, Árpád tér 2, Szeged, Hungary

³MTA-SZTE Biomimetic Systems Research Group, Department of Medical Chemistry, Faculty of Medicine, University of Szeged, H-6720, Dóm tér 8, Szeged, Hungary

⁴Department of Physical Chemistry and Materials Sciences, University of Szeged, H-6720, Aradi Vt. 1, Hungary

*mcsete@physx.u-szeged.hu

Abstract: Plasmonic bio-sensing chips were prepared by fabricating wavelength-scaled sinusoidal dielectric-metal interfacial gratings on polymer film covered bimetal layers. Lysozyme biomolecules (LYZ) and gold nanoparticle bioconjugates (AuNP-LYZ) were seeded onto the biochip surfaces. Comparison of the reflectance curves measured in a modified Kretschmann arrangement and computed numerically proved that monitoring of the narrower secondary reflectance minima under optimal rotated-grating coupling condition makes it possible to achieve enhanced sensitivity in biodetection. The enlarged reflectance minimum shift is due to the horizontally and vertically antisymmetric long-range plasmonic mode, which originates from surface plasmon polariton Bragg scattering and propagates at the border of the valley and hill. The sensitivity is significantly increased in case of bioconjugates due to the coupled localized resonances on the gold nanoparticles.

© 2017 Optical Society of America

OCIS codes: (280.1415) Biological sensing and sensors; (050.2770) Gratings; (160.4236) Nanomaterials; (240.6680) Surface plasmons.

References and links

1. S. I. Bozhevolnyi and T. Søndergaard, "General properties of slow-plasmon resonant nanostructures: nano-antennas and resonators," *Opt. Express* **15**(17), 10869–10877 (2007).
2. G. D'Aguanno, N. Mattiucci, A. Alú, and M. J. Bloemer, "Quenched optical transmission in ultrathin subwavelength plasmonic gratings," *Phys. Rev. B* **83**(3), 035426 (2011).
3. M. G. Weber and D. L. Mills, "Determination of surface-polariton minigaps on grating structures: A comparison between constant-frequency and constant-angle scans," *Phys. Rev. B Condens. Matter* **34**(4), 2893–2894 (1986).
4. W. L. Barnes, T. W. Preist, S. C. Kitson, J. R. Sambles, N. P. K. Cotter, and D. J. Nash, "Photonic gaps in the dispersion of surface plasmons on gratings," *Phys. Rev. B Condens. Matter* **51**(16), 11164–11167 (1995).
5. A. Ghoshal, I. Divliansky, and P. G. Kik, "Experimental observation of mode-selective anticrossing in surface-plasmon coupled metal nanoparticle arrays," *Appl. Phys. Lett.* **94**(17), 171108 (2009).
6. D. L. Mills, "Interaction of surface polaritons with periodic surface structures; Rayleigh waves and gratings," *Phys. Rev. B* **15**(6), 3097–3118 (1977).
7. M. Kretschmann, A. Leskova, and A. A. Maradudin, "Conical propagation of a surface plasmon polariton across a grating," *Opt. Commun.* **215**(4-6), 205–223 (2003).
8. M. Csete, C. Vass, J. Kokavecz, M. Goncalves, V. Megyesi, Zs. Bor, M. Pietralla, and O. Marti, "Effect of sub-micrometer polymer gratings generated by two-beam interference on surface plasmon resonance," *Appl. Surf. Sci.* **247**(1), 477–485 (2005).
9. M. Csete, G. Szekeres, C. Vass, N. Maghelli, K. Osvay, Zs. Bor, M. Pietralla, and O. Marti, "Surface plasmon resonance spectroscopy on rotated sub-micrometer polymer gratings generated by UV laser based two-beam interference," *Appl. Surf. Sci.* **252**(13), 4773–4780 (2006).
10. A. Szalai, G. Szekeres, J. Balázs, A. Somogyi, and M. Csete, "Rotated grating coupled surface plasmon resonance on wavelength-scaled shallow rectangular gratings," *Proc. SPIE* **8809**, 88092U (2013).

11. F. Romanato, L. K. Hong, H. K. Kang, C. C. Wong, Z. Yun, and W. Knoll, "Azimuthal dispersion and energy mode condensation of grating-coupled surface plasmon polaritons," *Phys. Rev. B* **77**(24), 245435 (2008).
12. E. Gazzola, L. Brigo, G. Zacco, P. Zilio, G. Ruffato, G. Brusatin, and F. Romanato, "Coupled SPP Modes on 1D Plasmonic Gratings in Conical Mounting," *Plasmonics* **9**(4), 867–876 (2014).
13. M. Perino, E. Pasqualotto, M. Scaramuzza, A. De Toni, and A. Paccagnella, "Characterization of Grating Coupled Surface Plasmon Polaritons Using Diffracted Rays Transmittance," *Plasmonics* **9**(5), 1103–1111 (2014).
14. S. Randhawa, M. U. González, J. Renger, S. Enoch, and R. Quidant, "Design and properties of dielectric surface plasmon Bragg mirrors," *Opt. Express* **18**(14), 14496–14510 (2010).
15. D. Kim, "Effect of the azimuthal orientation on the performance of grating-coupled surface-plasmon resonance biosensors," *Appl. Opt.* **44**(16), 3218–3223 (2005).
16. M. Csete, A. Köhási-Kis, V. Megyesi, K. Osvay, Zs. Bor, M. Pietralla, and O. Marti, "Coupled surface plasmon resonance on bimetallic films covered by sub-micrometer polymer gratings," *Org. Electron.* **8**(2), 148–160 (2007).
17. M. Csete, Á. Sipos, A. Köhási-Kis, A. Szalai, G. Szekeres, A. Mathesz, T. Csákó, K. Osvay, Zs. Bor, B. Penke, M. A. Deli, S. Veszelka, A. Schmatulla, and O. Marti, "Comparative study of sub-micrometer polymeric structures: dot-arrays, linear and crossed gratings generated by UV laser based two-beam interference, as surfaces for SPR and AFM based bio-sensing," *Appl. Surf. Sci.* **254**(4), 1194–1205 (2007).
18. Á. Sipos, H. Tóháti, A. Mathesz, A. Szalai, S. Veszelka, M. A. Deli, L. Fülöp, A. Köhási-Kis, M. Csete, and Zs. Bor, "Effect of nanogold particles on coupled plasmon resonance on biomolecule covered prepatterned multilayers," *Sens. Lett.* **8**(3), 512–520 (2010).
19. F. Romanato, K. H. Lee, H. K. Kang, G. Ruffato, and C. C. Wong, "Sensitivity enhancement in grating coupled surface plasmon resonance by azimuthal control," *Opt. Express* **17**(14), 12145–12154 (2009).
20. E. Gazzola, A. Pozzato, G. Ruffato, E. Sovernigo, and A. Sonato, "High-throughput fabrication and calibration of compact high-sensitivity plasmonic lab-on-chip for biosensing," *Opto-. Micro-. Nanofluid* **3**, 13 (2016).
21. M. Perino, E. Pasqualotto, M. Scaramuzza, A. De Toni, and A. Paccagnella, "Enhancement and control of surface plasmon resonance sensitivity using grating in conical mounting configuration," *Opt. Lett.* **40**(2), 221–224 (2015).
22. A. Shalabney and I. Abdulhalim, "Sensitivity-enhancement methods for surface plasmon sensors," *Laser Photonics Rev.* **5**(4), 571–606 (2011).
23. B. Spackova, P. Wrobel, M. Bocková, and J. Homola, "Optical biosensors based on plasmonic nanostructures: A Review," *Proc. IEEE* **104**(12), 2380–2408 (2016).
24. S. S. Senlik, A. Kocabas, and A. Aydinli, "Grating based plasmonic band gap cavities," *Opt. Express* **17**(18), 15541–15549 (2009).
25. C. Caucheteur, T. Guo, and J. Albert, "Review of plasmonic fiber optic biochemical sensors: improving the limit of detection," *Anal. Bioanal. Chem.* **407**(14), 3883–3897 (2015).
26. H. Shi, Z. Liu, X. Wang, J. Guo, L. Liu, L. Luo, J. Guo, H. Ma, S. Sun, and Y. He, "A symmetrical optical waveguide based surface plasmon resonance biosensing system," *Sens. Actuators B Chem.* **185**, 91–96 (2013).
27. S. Lal, S. Link, and N. J. Halas, "Nano-optics from sensing to waveguiding," *Nat. Photonics* **1**(11), 641–648 (2007).
28. B. Luk'yanchuk, N. I. Zheludev, S. A. Maier, N. J. Halas, P. Nordlander, H. Giessen, and C. T. Chong, "The Fano resonance in plasmonic nanostructures and metamaterials," *Nat. Mater.* **9**(9), 707–715 (2010).
29. K. Liu, X. Xue, and E. P. Furlani, "Theoretical Comparison of Optical Properties of Near-Infrared Colloidal Plasmonic Nanoparticles," *Sci. Rep.* **6**(1), 34189 (2016).
30. C. Formoso and L. S. Forster, "Tryptophan fluorescence lifetimes in lysozyme," *J. Biol. Chem.* **250**(10), 3738–3745 (1975).
31. H. Wei, Z. Wang, L. Yang, S. Tian, C. Hou, and Y. Lu, "Lysozyme-stabilized gold fluorescent cluster: Synthesis and application as Hg(2+) sensor," *Analyst (Lond.)* **135**(6), 1406–1410 (2010).
32. W. Y. Chen, J. Y. Lin, W. J. Chen, L. Luo, E. Wei-Guang Diao, and Y. C. Chen, "Functional gold nanoclusters as antimicrobial agents for antibiotic-resistant bacteria," *Nanomedicine (Lond.)* **5**(5), 755–764 (2010).
33. V. Hornok, E. Csapó, N. Varga, D. Ungor, D. Sebők, L. Janovák, G. Laczkó, and I. Dékány, "Controlled syntheses and structural characterization of plasmonic and red-emitting gold/lysozyme nanohybrid dispersions," *Colloid Polym. Sci.* **294**(1), 49–58 (2016).
34. H. Arwin, "Optical properties of thin layers of bovine serum albumin, γ -globulin, and hemoglobin," *Appl. Spectrosc.* **40**(3), 313–318 (1986).
35. P. B. Johnson and R. W. Christy, "Optical constants of the noble metals," *Phys. Rev. B* **6**(12), 4370–4379 (1972).
36. B. V. Derjaguin, V. M. Muller, and Y. P. Toporov, "On the role of molecular forces in contact deformations," *Colloid Interf. Sci.* **67**(2), 378–379 (1978).
37. M. Csete, G. Kurdi, J. Kokavecz, V. Megyesi, K. Osvay, Z. Schay Zs. Bor, and O. Marti, "Application possibilities and chemical origin of sub-micrometer adhesion modulation on polymer gratings produced by UV laser illumination," *Mater. Sci. Eng. C* **26**(5-7), 1056–1062 (2006).

1. Introduction

Surface plasmon polaritons (SPPs) propagating either on flat or on patterned surfaces have interesting far- and near-field properties. The characteristics of optical responses originating from short-range (SRSP) and long-range (LRSP) plasmonic modes, as well as from localized surface plasmon resonances (LSPR), that can be involved into the grating-coupling phenomena were analyzed in the literature [1, 2]. Presence of gratings results in opening of plasmonic band gaps (PBG) in those parameter regions, where Bragg scattering occurs [3, 4]. Caused by possible misinterpretation of the extrema at minigaps, it was concluded that to uncover PBGs a more reliable method is to plot the extrema as a function of frequency at a fixed angle of incidence [3, 4]. Band gap opening on the dispersion characteristics can originate from strong-coupling between localized and propagating modes as well, when the necessary condition of strong-coupling is the appropriate symmetry of interacting modes [5].

Significantly smaller amount of theoretical and experimental studies has been published about the effect of the periodic structures azimuthal orientation [6–14]. These studies initialized development of several novel plasmonic bio-sensing methodologies [14–20]. It was proven that the overlapping bands of modes supported by structured multilayers result in a plasmonic band gap at the Brillouin zone boundary [6,7]. In our previous studies we have presented the rotated grating-coupling surface plasmon resonance (RGC-SPR) occurring, when SPP excitation is performed in a conical mounting on a periodically structured multilayer, which is aligned onto a prism in a modified Kretschmann setup [8–10, 16–18]. Two SPPs with different wave vectors are excitable inside a narrow azimuthal orientation region, which result in double minima on the polar angle dependent reflectance [10]. However, in most of the studies on gratings in a conical mounting the light coupling is realized directly by the periodic structure [11–14, 19–21]. It was shown that two SPPs with the same wave vector, but having different propagation directions can be excited and result in reflectance minima in azimuthal orientations corresponding to the grating-coupled surface plasmon resonance (GCSPR) [11, 12, 19, 20]. The GCSPR phenomenon was demonstrated by monitoring transmittance maxima as well [12, 21]. It was proven that dielectric ridges on metal films in proper azimuthal orientation act as Bragg mirrors due to the large reflectance inside the band gap [14].

In recent nanophotonics there are tremendous efforts to overcome the limitations of conventional biosensors via SPR phenomena [15–26]. High sensitivity intra-cavity bio-sensing has been realized via cavity modes arising inside the PBGs on selectively loaded gratings [24]. An important application area of plasmon Bragg-gratings is bio-sensing, due to the enhanced sensitivity achievable via grating-coupled modes [25].

Application of grating-coupled SPR biosensors based on the monitoring of multiple diffracted orders in different azimuthal orientations is limited by the rotation sensitivity of the conical mounting [15]. In our previous experimental studies we have demonstrated that rotation into azimuthal orientations resulting in double reflectance minima also makes it possible to enhance the sensitivity in RGC-SPR based bio-sensing [16–18]. It was demonstrated that large sensitivity is achievable by monitoring either the reflectance minima or the transmittance maxima in GCSPR configuration [19–21]. The advantages of long-range modes, manifesting themselves in narrower extrema and accompanied by higher and spatially broader **E**-field enhancement, were also exploited [12, 26].

Novel class of localized surface plasmon resonance (LSPRS) bio-sensing methods relies on the sensitivity of LSPR to the presence of dielectric cover layers on plasmonic nano-objects [27–29]. At the same time, noble metal particles can play a multiple role, since they can enhance the local **E**-field intensity, accordingly they can be used as markers on SPP-based bioplatforms, moreover they can initiate cavity modes under certain circumstances.

Several intriguing biomolecules are fluorescent, among them lysozyme (LYZ) is an important protein having a potential to use in harmful material detection and in medicine. The

fluorescence of LYZ originates from tryptophan and sensitively depends on the chemical and dielectric environment [30].

Formation of biocompatible gold NCs can be promoted by adding LYZ into the aqueous solution of AuCl_4^- precursor. The spontaneous interaction of LYZ with the aurate ions results in formation of LYZ-stabilized Au NCs or Au NPs depending on the applied mass ratio of the reactants. Fluorescence of LYZ in clusters and in aggregates is retained, moreover, Au-LYZ complexes are sensitive to Hg concentration, which can be used in Hg detectors [31]. In addition to this, ~ 1 nm sized Au NCs as well as ~ 10 nm sized Au NPs coated by LYZ possess antimicrobial capabilities [32]. Recent studies revealed that 1:5 Au:LYZ mass ratio results in a protein shell around a NP core type bioconjugate, while in case of smaller ratios, Au NC seeds are distributed inside protein islands [33].

While preparing a plasmonic biosensor for specific fluorescent molecules, to achieve higher sensitivity in detection via SPR enhanced fluorescence phenomena it has to be ensured that the E-field enhancement is strong in those spectral intervals, where they absorb and emit light. However, precision tuning of SPP or LSPR phenomena into the excitation and emission bands, which strongly depend on bioconjugates composition is challenging, accordingly there is a great demand for alternate bio-sensing methodologies.

The purpose of our present work was to demonstrate that enhanced sensitivity is achievable by monitoring the reflectance minima arising due to rotated grating-coupling phenomenon in a narrow azimuthal orientation region. Another purpose was to answer the question, whether sensitivity to LYZ protein can be further increased by using AuNP-LYZ bioconjugates in RGC-SPR based biodetection. Experimental reflectance curves observed via angle interrogation of RGC-SPR phenomenon were compared to reflectance curves determined by numerical computations. The accompanying near-field distribution was inspected to uncover the underlying nanophotonical phenomena. Further computations were performed to demonstrate the existence of an optimal configuration, which has potential to achieve maximal polar angle shift and extremely large sensitivity and figure of merit (FOM). The dispersion characteristics of the responsible grating-coupled SPPs was mapped, and a general methodology is proposed, which makes it possible to achieve enhanced sensitivity via grating-based bio-sensing chips in an optimal conical mounting.

2. Methods

2.1. Experimental methods

2.1.1. Preparation of plasmonic AuNP-LYZ nanodispersions

For the preparation of LYZ reduced Au NPs, LYZ ($\geq 90\%$, Sigma-Aldrich), $\text{HAuCl}_4 \cdot 3\text{H}_2\text{O}$ ($\geq 49.0\%$, Sigma-Aldrich) and sodium hydroxide (99%, Molar Chemicals) were used. During preparation LYZ solution with 0.98 mg/mL concentration and 10 mL of HAuCl_4 solution with 1.0 mM concentration were admixed. The appropriate pH 12 was adjusted with 2 M NaOH solution. After 18 h incubation at 40 °C the color modification of the solution indicated the Au NPs formation. Different AuNP-LYZ bioconjugates were synthesized and the diameter of NPs was altered by tuning the fraction of LYZ. Dispersions prepared with a ratio of $m_{\text{Au}}:m_{\text{LYZ}} = 1:5$ became red color, indicating LSPR related absorptance close to the 532 nm wavelength of SPR interrogation (Fig. 1(a)). Accordingly, this dispersion was selected for RGC-SPR sensing of bioconjugates.

2.1.2. Characterization of AuNP-LYZ bioconjugates

Transmission electron microscopy (TEM) was used to visualize the Au NPs with a Technai (200 kV) apparatus and then the size of bioconjugates was estimated based on the TEM images (UTHSCSA Image Tool 2.00 software) (Fig. 1(a), inset). The measurement of the absorption spectrum was carried out with UVIKON 930 type dual-beam spectrophotometer.

The emission spectrum was measured with Horiba Jobin Yvon Fluoromax-4 spectrofluorimeter with 365 nm excitation wavelength and the width of the slit was 3 nm (Fig. 1(a)).

2.1.3. Experimental investigation of RGC-SPR

For biochip preparation the NBK7 glass substrates were evaporated by 38 nm thick silver and 7 nm thick gold films. Bimetal layer is necessary to realize efficient plasmon coupling, since silver has good plasmonic properties, while the thin gold cover-layer protects the silver from corrosion [8–10, 16–18]. A polycarbonate (PC) layer with ~65 nm thickness was spin-coated onto the bimetal surfaces, and one dimensional gratings with a sinusoidal profile were fabricated via two-beam interference laser procedure (Figs. 1(b)-1(e)). In our previous studies it was shown that at 532 nm excitation rotated grating-coupling of SPPs occurs on the wavelength-scaled $p = 416$ nm periodic PC grating covered bimetal layer, when the a modulation amplitude is larger than a minimal value determined by the multilayer composition [16]. The thinnest average PC layer is 15.75 nm, which makes it possible to achieve a good coupling efficiency on a grating with $2a > 31.5$ nm modulation depth [8–10, 16–18].

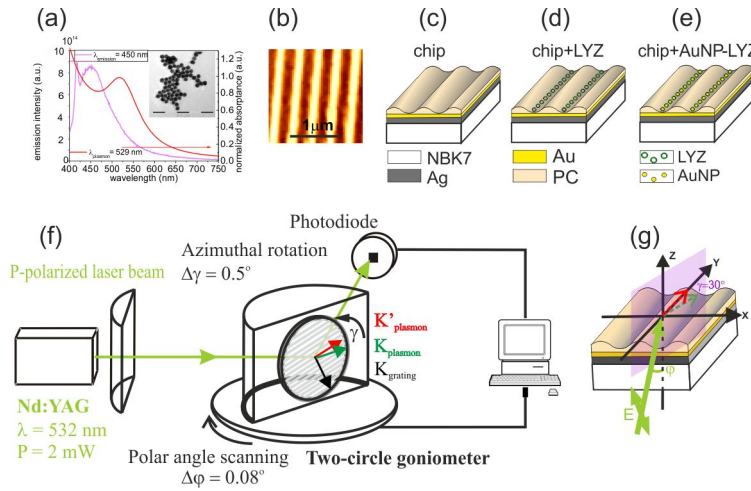


Fig. 1. (a) Absorbance and emission spectra of AuNP-LYZ nanodispersions with $m_{Au}:m_{LYZ} = 1:5$ mass ratio, the inset shows TEM image of the AuNP-LYZ bioconjugates, (b) AFM picture of the 416 nm periodic grating surface. Schematic drawings of the investigated biosensor chips: (c) sinusoidal polymer grating, (d) sinusoidal grating covered by LYZ biomolecules and (e) sinusoidal grating covered by AuNP-LYZ bioconjugates. (f) Schematic drawing of the SPR setup based on a modified Kretschmann arrangement, used to study the RGC-SPR phenomenon. (g) Method of ϕ polar and γ azimuthal angle tuning.

The 10 mJ/cm^2 laser fluence applied in biochip preparation ensured that the polymer grating modulation depth was approximately double of the minimal value, accordingly the rotated grating-coupling condition was fulfilled. For RGC-SPR based biodetection measurements LYZ biomolecule and AuNP-LYZ bioconjugate containing solutions were seeded onto the structured multilayers (Figs. 1(c)-1(e)). The angle interrogation of the RGC-SPR was performed in a modified Kretschmann arrangement by varying the polar angle with $\Delta\phi = 0.08^\circ$ steps (Fig. 1(f)). The 532 nm p-polarized light was coupled into SPPs (K_{plasmon}) via a half-cylinder, while the efficient grating-coupled SPP mode (K'_{plasmon}) excitation was ensured by the azimuthal rotation of the substrate. The azimuthal orientation of the grating grooves with respect to the plane of incidence was set to $\gamma \sim 30^\circ$ via special holders, which ensured rotation with $\pm 0.5^\circ$ accuracy (Figs. 1(f) and 1(g)). A frequency doubled Nd:YAG

laser (Intelite, GSLN32-20, $\lambda = 532$ nm, 2 mW) was used to realize SPP excitation. The reflected light was collected by a standard visible range photodetector (Thorlabs DET 110).

To ensure the appropriate φ - 2φ rotation of the half-cylinder and the photodetector, a two-circle goniometer (OWIS, with DMT 65, 2-Ph-SM 240) was used. The RGC-SPR phenomenon was angle interrogated first on bare chips for reference purposes, then on a sensor-chip covered by LYZ, and finally the effect of AuNP-LYZ bioconjugates was studied (Figs. 1(c)-1(e)). The measured reflectance curves are presented in Fig. 2(a) with insets.

2.2. Theoretical methods

Numerical computations were carried out with COMSOL Multiphysics software package (COMSOL AB) based on Finite Element Method (FEM). Radio Frequency Module was used to calculate reflectance from the structured multilayer in a conical mounting. The electromagnetic near-field distribution was also inspected at the resonances manifesting themselves in reflectance minima, in order to uncover the characteristics of SPP modes that are at play in grating-coupling. Both the normalized \mathbf{E} -field and the E_y field component were studied in the horizontal and vertical plane cross-sections of the unit cells of the inspected gratings. The vertical plane cross-section along the valley was taken at the turning line in the horizontal cross-section of the E_y field component. The intersection of the vertical plane through the turning line of the E_y field component and the grating surface is referred as the border of the valley and hill. Since the E_y is the longitudinal component of the modes propagating along the stripes, its analyses allows determination of the symmetry properties of SPPs coupled in specific RGC-SPR illumination configurations.

The wavelength-dependent optical properties of all components were taken into account. The refractive index of LYZ was considered by the usual Cauchy-formula of proteins ($n_{LYZ} = AC + BC / \lambda^2$, where $AC = 1.45$, $BC = 0.01\text{m}^2$) according to the literature [34]. The wavelength-dependent complex dielectric functions of Au and Ag layers were implemented based on the literature, by interpolating the measured data sets with spline-fits [35].

2.2.1. Numerical modeling of RGC-SPR on a fitted chip

The modeling of a fitted chip was realized to analyze the effect of the multilayer composition, illumination direction, protein location on the reflectance and to uncover the physical origin of the reflectance minima arising during RGC-SPR, by analyzing the accompanying near-field phenomena (Fig. 2(b), Fig. 3, Fig. 8). The fitted chip is an artificial multilayer with a fitted sinusoidal grating profile and an azimuthal orientation, which results in reflectance minima at polar angles approximating the measurements. First the reflectance curves measured on bare chips were fitted by varying the modulation depth as well as by tuning the azimuthal orientation of a sinusoidal PC grating (Figs. 1(c), 2(b)). Then the reflectance curve measured on a LYZ covered chip was fitted, by varying the dielectric layer thickness only at the bottom of the grating valley (Figs. 1(d), 2(b)). Assumption of LYZ location inside the valley is in accordance both with theoretical computations and with AFM measurements, which prove the existence of a sinusoidal adhesion modulation of topography origin [36, 37]. The sinusoidal adhesion modulation promotes the adherence of bio-bio-objects inside the valleys of the polymer gratings [16–18, 37]. The equivalent protein layer thickness was computed by taking into account that the PC and LYZ layers have different dielectric properties.

The biomolecules and bioconjugates were included into the COMSOL models by aligning linear arrays of hollow LYZ shells and AuNP-LYZ core-shell particles along the grating valley (Figs. 1(d) and 1(e)). The 13.4 nm common core diameter was selected based on the size distribution of AuNPs measured on TEM images (Fig. 1(a), inset). The 1.8 nm thickness of LYZ shell was set based on the thickness of monomolecular covering. Accordingly, multiple arrays of hollow LYZ shells with 6.7 nm and 8.5 nm inner and outer radii and a total

volume corresponding to the previously fitted protein layer thickness were aligned at the bottom of the valley (Fig. 1(d)).

By taking into account that the gold NPs presence may alter the amount of biomolecules adhered from a dispersion, such a different number of core-shell particles consisting of AuNP cores covered by LYZ shells was selected, which ensured a reflectance minimum shift corresponding to the measurement on the bioconjugates covered chip (Fig. 1(e)).

In our previous studies an adhesion enhancement of non-topographical origin was also demonstrated at the border of the valleys and hills of polycarbonate gratings prepared by two-beam interference [16–18, 37]. Accordingly, both the LYZ biomolecule and AuNP-LYZ bioconjugate arrays were relocated from the bottom of the valley to the hillside, to prove the existence of a preferred location, where the sensitivity can be further enhanced (Fig. 2(b), Fig. 3, Fig. 8). The exact location of the LYZ and AuNP-LYZ arrays on the hillside was selected by taking into account the distribution of the normalized E -field and of the E_y field component on the bare chip, as it is described in **Section 3.3** and in the **Appendix**. The normalized E -field and the E_y field component distribution was studied in the horizontal and vertical plane cross-sections of one unit cell of the fitted chip (Fig. 3, Fig. 8). The reflectance minima are referred as dips in those paragraphs, where the E -field spatial distribution is described, in order to avoid confusion. The reflectance was computed in the fitted azimuthal orientation of the fitted chips by varying the polar angle in $[38^\circ, 78^\circ]$ interval with 1° steps, while higher 0.01° resolution was applied at the reflectance minima (Fig. 2(b)).

The $S_\phi = \Delta\phi/\Delta n_{\text{effective}}$ sensitivity and $FOM = \Delta\phi/(\Delta n_{\text{effective}} FWHM_{\text{average}})$ values were determined for both bio-object locations, by taking into account the $\Delta n_{\text{effective}}$ effective refractive index modification corresponding to the dielectric LYZ and to the composite AuNP-LYZ layers [22, 23]. The $\Delta n_{\text{effective}}$ modification corresponding to AuNP-LYZ was determined based on effective medium theory, and the decay length of the E -field was supposed to be equal to that at the multilayer-air interface (Table 1). A calibration plot was determined to compare the concentration dependence of the polar angle shift, sensitivity and FOM of the secondary and primary reflectance minima (Fig. 7 in Appendix).

2.2.2. Numerical modeling of RGC-SPR on a designed chip

Detailed theoretical study of a designed biochip has been performed as well to demonstrate the RGC-SPR phenomenon in an optimal configuration (Figs. 2(c)-2(e), Fig. 4, Fig. 5, Fig. 6, Fig. 9). The designed chip is an artificial multilayer consisting of a sinusoidal grating profile, the parameters of which approximate the minimal average polymer layer thickness and modulation depth capable of resulting in RGC-SPR phenomenon in case of the applied multilayer composition. The reflectance was studied on different multilayers by varying the polar angle in $[38^\circ, 78^\circ]$ interval and by tuning the azimuthal orientation in $[28^\circ, 38^\circ]$ interval, both with 1° steps (Figs. 2(c)-2(e) and Fig. 4). Higher 0.01° polar angle resolution was applied to determine the exact polar angles corresponding to the reflectance minima. For angle interrogation of the SPR the optimal orientation of a biochip with a specific multilayer composition is qualified by the azimuthal angle, which makes it possible to achieve the maximal polar angle shift. The reflectance of bare chips, and biochips covered by LYZ biomolecule and AuNP-LYZ bioconjugate were compared for three representative azimuthal orientations to prove the existence of an optimal orientation (Figs. 2(c)-2(e), Fig. 4).

The sensitivity and FOM values achievable in case of LYZ and AuNP-LYZ detection on the designed chip were compared to the sensitivity and FOM values of conventional SPP and LSPR biosensors and to the corresponding characteristic values reached via the fitted chip (Table 1) [22, 23].

To analyze the spatial overlap between the coupled modes and bio-objects, the normalized E -field and the E_y field component were studied in the horizontal and vertical plane cross-

sections of two unit cells of the periodic structure on the designed chip (Fig. 5, with corresponding Visualization 1, Fig. 9).

The purpose was to show that the optimal configuration makes it possible to improve the spatial overlap between the grating-coupled SPPs and the bio-objects at the bottom of the grating valley, where the adhesion modulation of topography origin inherently promotes their adherence [16–18, 37].

In order to explain the nanophotonical origin of the coupled reflectance minima, the dispersion characteristics of bare, LYZ and AuNP-LYZ coated designed biochips were determined as well (Fig. 6). The wavelength was swept in [300 nm, 700 nm] interval with 10 nm steps, while the polar angle was swept in [38°, 78°] interval with 1° steps.

3. Results and discussion

Based on TEM measurements the average diameter of AuNP-LYZ particles in the dispersion with $m_{Au}:m_{LYZ} = 1:5$ mass ratio was ~13.4 nm. The spectral study revealed that this dispersion exhibits a fluorescence with an emission maximum at 450 nm in case of excitation at 365 nm, and has a well-defined absorption at 529 nm, which is close to the 532 nm wavelength used for SPP excitation (Fig. 1(a)). Accordingly, all SPP coupling phenomena, which result in EM-field enhancement at this wavelength, promote the bioconjugates absorption and mediate increase the sensitivity to them. As a result, the fluorescent AuNP-LYZ bio-conjugates can be sensitively detected by SPR interrogation also outside their excitation and emission bands.

3.1. Experimental demonstration of RGC-SPR

The experimental RGC-SPR studies revealed that double reflectance minima are observable in $\gamma \sim 30^\circ$ azimuthal orientation on multi-layers consisting of $p = 416$ nm periodic polycarbonate gratings with $2a \sim 65.00$ nm modulation depth. The applied nominations reveal that the secondary reflectance minimum is in the region of smaller polar angles, while the primary reflectance minimum resembles to that originating from SPPs on a flat multilayer surface. All azimuthal and polar angles corresponding to reflectance minima are collected in Table 1 provided in the Appendix.

The secondary minima appear at $\phi_{chip_1}^{secondary} = 52.16^\circ$ and $\phi_{chip_2}^{secondary} = 50.72^\circ$ polar angles on the studied bare biochips (Fig. 2(a)). Covering by LYZ causes a secondary minimum at $\phi_{chip_1+LYZ}^{secondary} = 52.48^\circ$ polar angle, which corresponds to a moderate $\Delta\phi_{chip_1+LYZ}^{secondary} = 0.32^\circ$ shift in polar angle. Covering by AuNP-LYZ results in a secondary minimum at $\phi_{chip_2+AuNP-LYZ}^{secondary} = 51.6^\circ$, which indicates a more than two-times larger $\Delta\phi_{chip_2+AuNP-LYZ}^{secondary} = 0.88^\circ$ polar angle shift. These results unambiguously prove that presence of Au NPs results in a significantly larger shift of the secondary minimum. The measurements also indicate that the observation possibility of both minima sensitively depends on the exact multilayer composition (Fig. 2(a)). Namely, in $\gamma \sim 30^\circ$ azimuthal orientation the primary minimum at $\phi_{chip_1}^{primary} = 64.96^\circ$ is flattened and shifted backward by a small $\Delta\phi_{chip_1+LYZ}^{primary} = -0.76^\circ$ polar angle, when only LYZ is adhered to the surface, while the secondary minimum is still suitable for detection. In contrast, the primary minimum at $\phi_{chip_2}^{primary} = 69.44^\circ$ is preserved during the adherence of AuNP-LYZ, it is shifted backward by a large $\Delta\phi_{chip_2+AuNP-LYZ}^{primary} = -4.8^\circ$ polar angle, but at the same time it is significantly broadened. The decrease of the corresponding polar angles and the significantly larger FWHMs indicate that the primary minima are less suitable for detection via RGC-SPR monitoring (Fig. 2(a)).

The sensitivity and FOM values corresponding to the measurements in case of LYZ seeding are commensurate with those published for SPP and LSPR biochips, respectively.

In contrast, in case of AuNP-LYZ both the sensitivity and the FOM values are larger than those achievable via special grating based methods, e.g. via GCSRP [19, 22, 23]. These results indicate that it is reasonable to apply the RGC-SPR phenomenon for biosensing.

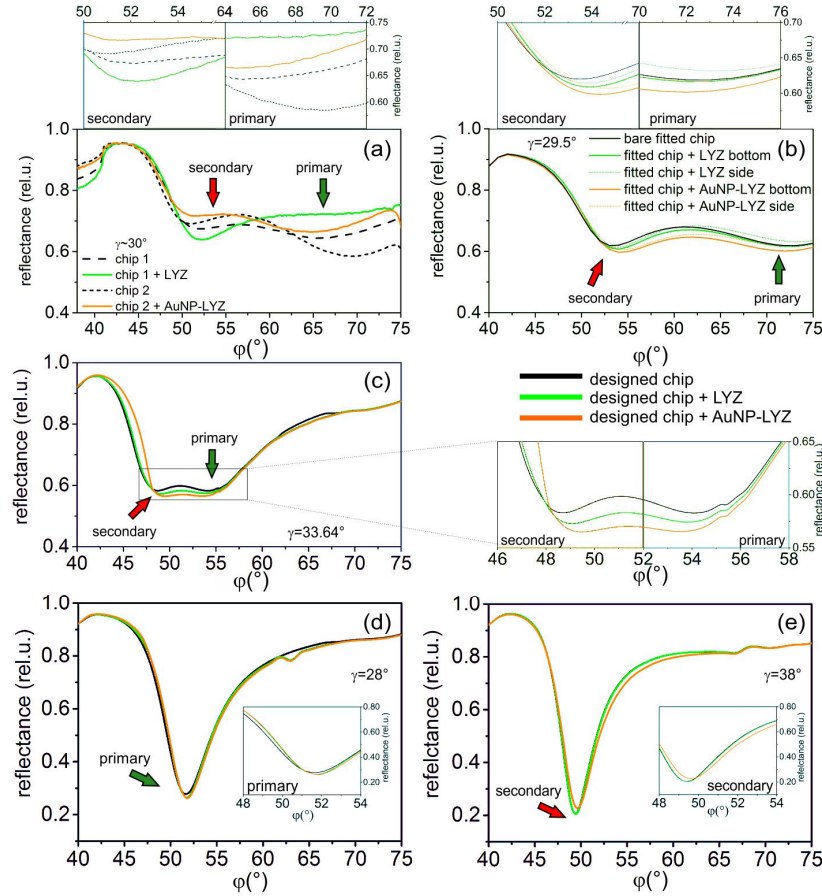


Fig. 2. Reflectance before and after covering by LYZ biomolecules and AuNP-LYZ bioconjugates (a) measured on two sensor chips, (b) computed on the fitted sensor chip in case of bio-objects at the bottom of valley and on the side of the hill, (c-e) computed on the designed sensor chip in case of bio-objects at the bottom of valley in different azimuthal orientations: (c) $\gamma = 33.64^\circ$; (d) $\gamma = 28^\circ$; (e) $\gamma = 38^\circ$. The insets indicate the magnified reflectance curves around the reflectance minima.

3.2. Modeling reflectance governed by RGC-SPR on the fitted chip

Based on the fitting of surface profiles on uncovered chips, the modulation depth on both multilayers is $2a_{\text{fitted_chip_1}} \sim 2a_{\text{fitted_chip_2}} \sim 63$ nm. The fitted azimuthal orientation is $\gamma_{\text{fitted_chip}} \sim 29.5^\circ$, which almost equals to the $\gamma_{\text{multilayer_optimal}} = 29.3^\circ$ optimal azimuthal orientation computed for the fitted multilayer composition based on reference [16].

By supposing that both the LYZ biomolecules and AuNP-LYZ bioconjugates are seeded exactly at the bottom of the valley, adherence of $N_{\text{fitted_chip+LYZ_bottom}} = 120$ number of LYZ shells and $N_{\text{fitted_chip+AuNP-LYZ_bottom}} = 16$ number of AuNP-LYZ core-shells per one unit cell results in $\Delta\phi_{\text{fitted_chip+LYZ_bottom}}^{\text{secondary}} = 0.4^\circ$ and $\Delta\phi_{\text{fitted_chip+AuNP-LYZ_bottom}}^{\text{secondary}} = 0.9^\circ$ secondary minimum shifts, which are slightly larger than the measured shifts (Fig. 2(b)). The same amount of

biomolecules and bioconjugates per unit cell causes $\Delta\phi_{\text{fitted_chip+LYZ_bottom}}^{\text{primary}} = -0.2^\circ$ and $\Delta\phi_{\text{fitted_chip+AuNP-LYZ_bottom}}^{\text{primary}} = -0.6^\circ$ primary minimum backward shift, respectively (Fig. 2(b)).

By supposing that the biomolecules and bioconjugates adhere on the hillside, there are various representative locations. The most interesting are the $x = 301.5$ nm hillside location of the 120 LYZ biomolecules and the $x = 285$ nm location of the linear array of 16 AuNP-LYZ bioconjugates, which result in the largest secondary resonance minimum shift.

The sensitivity of the secondary minimum is considerably enhanced at these locations, namely the same number of $N_{\text{fitted_chip+LYZ_side}} = 120$ LYZ shells and $N_{\text{fitted_chip+AuNP-LYZ_side}} = 16$ number of AuNP-LYZ core-shells per unit cell results in $\Delta\phi_{\text{fitted_chip+LYZ_side}}^{\text{secondary}} = 0.5^\circ$ and $\Delta\phi_{\text{fitted_chip+AuNP-LYZ_side}}^{\text{secondary}} = 1.1^\circ$ shift of the corresponding secondary minimum (Fig. 2(b)). These shifts are more significantly larger than the measured values. The same amount of LYZ biomolecules and AuNP-LYZ bioconjugates per unit cell causes $\Delta\phi_{\text{fitted_chip+LYZ_side}}^{\text{primary}} = 0.3^\circ$ and $\Delta\phi_{\text{fitted_chip+AuNP-LYZ_side}}^{\text{primary}} = -0.4^\circ$ primary minimum shift, respectively (Fig. 2(b)). By supposing adherence on the hillside instead at the valley-bottom, both the secondary and primary minimum is shifted by a larger degree in case of LYZ. In contrast, a larger secondary minimum forward shift and a smaller primary minimum backward shift is achieved via AuNP-LYZ relocation onto the hillside.

Important advantage of the secondary minimum that its larger sensitivity and smaller FWHM ensures considerably larger FOM, which is further enhanced in case of hillside location (Table 1). In contrast, the larger forward shift of the primary minimum in case of hillside LYZ adherence is accompanied by a significant broadening, which allows a slightly smaller FOM. Moreover, the smaller primary minimum backward shift manifests itself in a smaller sensitivity and FOM in case of AuNP-LYZ adherence on the hillside (Table 1). These results reveal again that the primary minimum monitoring is less suitable for biodetection.

Explanation of the larger sensitivity and FOM values achievable by monitoring the secondary minima, which parameters are significantly improved in presence of Au NPs, and the explanation of the weaker parameters of corresponding primary minima in all inspected configurations of the fitted chip are described in **Section 3.3** and in the **Appendix**. Concentration dependence of the polar angle shift, sensitivity and FOM values corresponding to the secondary and primary reflectance minima in case of LYZ and AuNP-LYZ location at the bottom of the valley and on the side of the hill is presented in Fig. 7 in the **Appendix**.

3.3. Near-field distribution on the fitted chip

In 29.5° azimuthal orientation of the bare fitted chip the **E**-field distribution indicates a global maximum on the left side of the valley at both reflectance dips. However, at the secondary dip the global maximum is shifted with a larger extent towards the valley center, and there is a local maximum on the right side of the valley (Fig. 2(b), Figs. 3(a) and 3(b)/a-to-d, right, Figs. 8(a) and 8(b)/a-to-d, left). The E_y field component is antisymmetrical horizontally at both dips, however the turning line is shifted with a larger extent towards the succeeding hill at the secondary dip (3(a) and 3(b)/a-to-d, left, $x = 375$ nm to $x = 275$ nm). In the vertical cross-section taken along the valley the E_y field component is antisymmetrical (slightly hybrid) at the secondary (primary) dip (Figs. 3(a) and 3(b)/a-to-d, middle). Similarly, in the vertical cross-section taken perpendicularly to the grating the E_y field component is antisymmetrical (slightly hybrid) at the secondary (primary) dip (Figs. 8(a) and 8(b)/a-to-d, right). Comparison of the E_y field distributions confirms that a LRSPP possessing a horizontally and vertically antisymmetric longitudinal component propagates along the right border of the valley and hill at the secondary dip, while at the primary dip the hybrid E_y components reveal that a SRSPP mode exists. The LRSPPs possess a small attenuation due to the small overlap with the metal layer [12, 26]. Accordingly, larger interaction cross-section is expected at the secondary dip

with the biomolecules and bioconjugates, which is capable of improving the sensitivity and FOM significantly.

Attachment of bio-objects shifts the reflectance dips, and transforms the near-field distribution as well. At all reflectance dips appearing in $\gamma = 29.5^\circ$ azimuthal orientation after seeding by LYZ biomolecules and AuNP-LYZ bioconjugates the area corresponding to the global the \mathbf{E} -field maximum is similarly coincident with the left side of the valley. However, at the secondary dips the global \mathbf{E} -field maximum is shifted towards the succeeding hill with a larger extent, and is accompanied by a local maximum at the right side of the valley, similarly to the bare biochips (Fig. 2(b), Figs. 3(a) and 3(b)/b,c-to-e,f, right, Figs. 8(a) and 8(b)/ b,c-to-e,f, left). The local \mathbf{E} -field enhancement is larger in presence of Au NPs for both bio-object locations (Figs. 3(a) and 3(b)/b,e-to-c,f, right, Figs. 8(a) and 8(b)/b,e-to-c,f, left and middle).

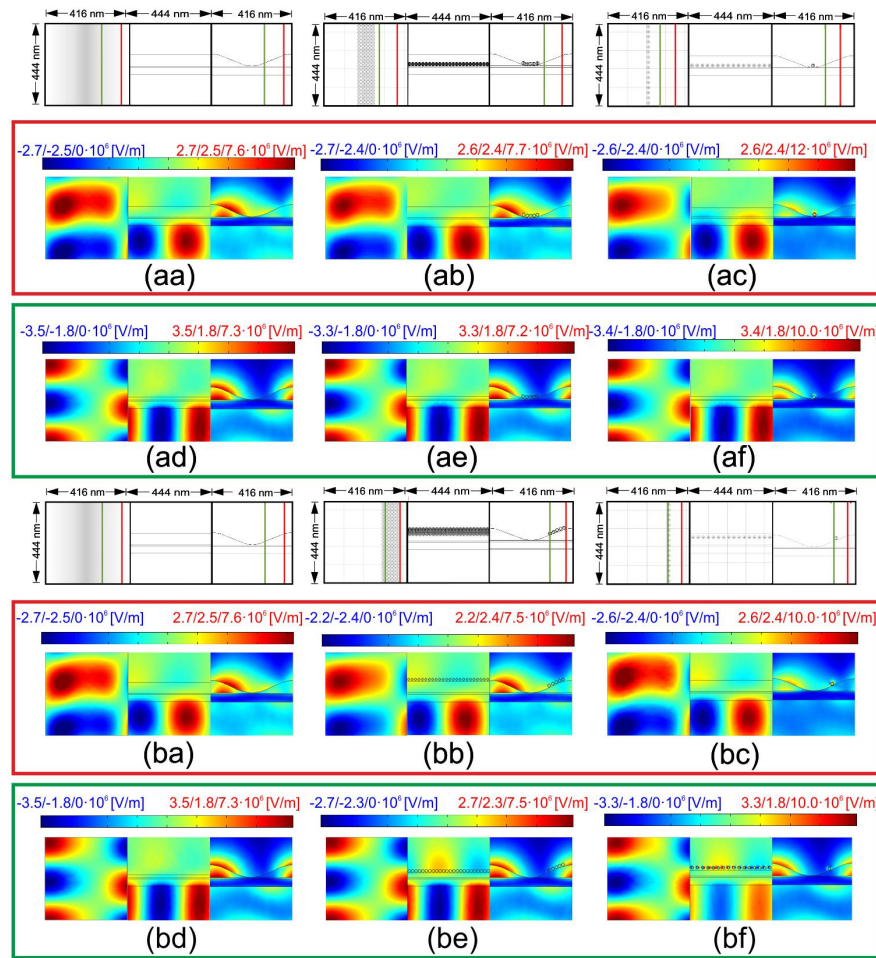


Fig. 3. The E_y field component in planes taken horizontally (x-y plane: left) and vertically along the valley at the turning line of E_y (y-z plane: middle) and the normalized (\mathbf{E})-field distribution perpendicular to the unit cell (x-z plane: right) on (a,b/ a,d) bare fitted chip, (a,b/ b,e) fitted chip covered by LYZ biomolecules, (a,b/ c,f) fitted chip covered by AuNP-LYZ bioconjugates, in 29.5° azimuthal orientation of the fitted chip (a,b/ a-c) secondary and (a,b/ d-f) primary minima in case of bio-objects (a/ a-f) at the bottom of valley and (b/ a-f) on the side of the hill. The schematic drawings indicate the structure contours in different plane cross-sections and the turning lines of the E_y field component at the secondary (red) and primary (green) reflectance minima.

At the secondary dips observable after LYZ and AuNP-LYZ covering the turning line of the antisymmetric E_y longitudinal component is backward shifted ($x = 364$ nm and $x = 350$ nm) with respect to that on the bare chip ($x = 375$ nm), when the bio-objects are at the bottom of the valley, while it is forward shifted in case of bio-object location on the side of the hill ($x = 380$ nm and $x = 387$ nm) (Figs. 3(a) and 3(b)/b and c, left). At all secondary dips the E_y longitudinal component is antisymmetrical in the vertical cross-section taken along the valley (Figs. 3(a) and 3(b)/b and c, middle). In contrast the E_y longitudinal component is slightly hybrid perpendicularly to the unit cell for both biomolecules and bioconjugates locations (Figs. 8(a) and 8(b)/b and c, right).

These near-field phenomena prove that a horizontally and vertically antisymmetric LRSP mode exists at all secondary dips. The advantage of the bio-objects hillside location is that they approach the turning line of the E_y component, where the antisymmetry is two-fold, moreover they overlap with the local normalized E -field maximum on the right side of the valley, which makes it possible to maximize the interaction cross-section with the LRSP.

The secondary dip shift exhibits a location dependence according to the expectations, namely slightly larger shift and sensitivity as well as FOM was observed in case of hillside location for both bio-coverings (Fig. 2(b), Table 1). At the secondary dips arising after LYZ covering, location of the 120 LYZ biomolecules per unit cell at the bottom of the valley ensures compromised overlap with both the global and local E -field maxima, while on the hillside perfect overlap of multiple LYZ arrays is ensured with the local E -field maximum at the right side of the valley (Figs. 3(a) and 3(b)/b, right). As a result, the secondary dip exhibits the largest sensitivity, when the central array of 120 LYZ islands is relocated to the optimal location ($x = 301.5$ nm) on the hillside. In contrast, location of the 16 AuNP-LYZ bioconjugates at the bottom of valley ensures smaller overlap with both of the global and local E -field maxima, while at the optimal location ($x = 285$ nm) on the hillside perfect overlap is ensured for the single AuNP-LYZ array with the local E -field maximum corresponding to the horizontally and vertically antisymmetric LRSP (Figs. 3(a) and 3(b)/c right). Presence of AuNPs results in additional local E -field enhancement both at the bottom of the valley and on the side of the hill. This explains that significantly smaller amount of AuNP-LYZ can be detected by monitoring the secondary dip (Figs. 3(a) and 3(b)/c right, Figs. 8(a) and 8(b)/c left, middle).

At the primary dips the turning line of the antisymmetric E_y longitudinal component is unmodified with respect to that on bare chip ($x = 275$ nm) in case of LYZ biomolecules and AuNP-LYZ bioconjugates location at the bottom of the valley, while the turning line is noticeably forward shifted ($x = 295$ nm and $x = 305$ nm), when the bio-objects are on the hillside (Figs. 3(a) and 3(b)/e and f, left). For both coverings by LYZ and AuNP-LYZ the E_y longitudinal component is hybrid (antisymmetrical) in the vertical cross-section taken along the valley in case of bio-object location at the bottom of the valley (on the side of the hill) (Figs. 3(a) and 3(b)/e, f middle). In contrast, the E_y longitudinal component is hybrid perpendicularly to the unit cell (Figs. 8(a) and 8(b)/e, f right). These near-field phenomena prove that at the primary dips for both coverings by LYZ biomolecules and AuNP-LYZ bioconjugates a SRSP exists, when the bio-objects are located at the bottom of the valley, while a horizontally and vertically antisymmetric LRSP is coupled in case of hillside location.

At the primary dips location of 120 LYZ biomolecules at the bottom of the valley cannot ensure overlap with the global E -field maxima on either of the neighboring hills, while in case of hillside location overlap is ensured with both the turning line of the antisymmetric E_y at the border of the valley and hill and with the global normalized E -field maximum on the succeeding hill (Figs. 3(a) and 3(b)/e, right). Accordingly, the primary dip exhibits an enhanced shift, when the central array of the wide 120 LYZ islands is relocated to $x = 301.5$ nm on the hillside (Fig. 2(b), Table 1). Moreover, the primary dip exhibits a backward shift in case of LYZ location at the bottom of valley, while a larger forward shift is observable in case

of LYZ location on the hillside. The sensitivity is enhanced, while the FOM is slightly decreased caused by relocation, despite the presence of LRSPP. The FOM decrease is caused by the increased FWHM of the reflectance minimum.

Location of the 16 AuNP-LYZ biomolecules at the bottom of the valley cannot ensure good overlap with the global \mathbf{E} -field maxima on either of the neighboring hills, while relocation onto the hillside completely prevents the overlap with the global \mathbf{E} -field maximum on the preceding hill, and does not make possible noticeable overlap with the \mathbf{E} -field maximum on the succeeding hill (Figs. 3(a) and 3(b)/f, right). As a consequence, when 16 AuNP-LYZ bioconjugates are located to $x = 285$ nm on the hillside the primary dip exhibits a backward shift, which is slightly reduced with respect to that in case of AuNP-LYZ location at the bottom of valley. Both the sensitivity and the FOM of the primary dip are smaller in case of AuNP-LYZ hillside location despite the presence of LRSPP (Fig. 2(b), Table 1).

In summary, at both of the secondary and primary dips the 120 LYZ biomolecules are moved into the \mathbf{E} -field maxima on the succeeding hill in case of hillside location, which results in increased sensitivity compared to that achievable, when the biomolecules are at the bottom of the valley. The 16 AuNP-LYZ bioconjugates are closer to the turning line of the E_y component on the hillside, and properly overlap with the local \mathbf{E} -field maximum at the secondary dip, while do not coincide with the global \mathbf{E} -field maximum on the succeeding hill at the primary dip. As a consequence, the secondary dip exhibits a larger sensitivity and FOM, while the primary dip has a smaller sensitivity and FOM in case of hillside location of the AuNP-LYZ bioconjugates. Accordingly, at the primary dip a smaller shift and a corresponding smaller sensitivity and FOM is achievable with respect to those at the secondary dip at both bio-object locations on the fitted chip.

3.4. Modeling reflectance governed by RGC-SPR on the designed chip

To prove that the enhanced sensitivity experienced in presence of a horizontally and vertically antisymmetric LRSPP is a general phenomenon, and a maximal enhancement is achievable in an optimal configuration, inspection of a designed chip with a minimal modulation depth corresponding to the condition of rotated grating-coupling has been also performed.

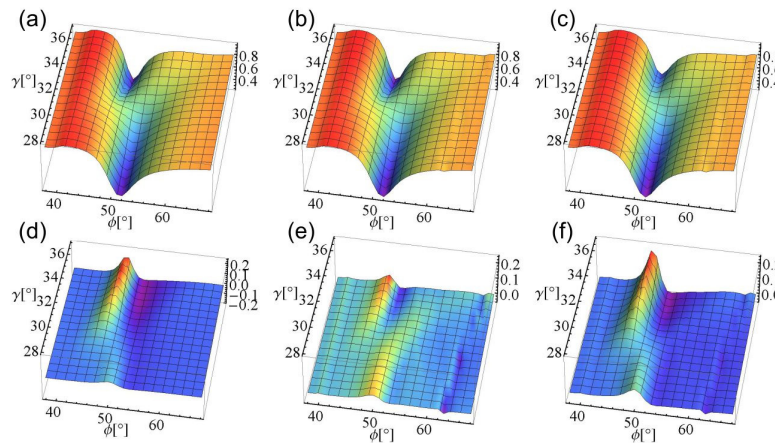


Fig. 4. Calculated reflectance of different chips as a function of polar angle ($\varphi = [28^\circ, 78^\circ]$) and azimuthal orientation ($\gamma = [28^\circ, 38^\circ]$): (a) bare designed chip, (b) designed chip covered by 8 LYZ biomolecules per unit cell and (c) designed chip covered by 8 AuNP-LYZ bioconjugates per unit cell. (d) Difference between reflectance modifications in case of different coverings; (e, f) reflectance modification caused by (e) 8 LYZ biomolecules and (f) 8 AuNP-LYZ bioconjugates per unit cells covering of the designed chip, compared to the bare designed chip.

In order to compare the azimuthal orientation dependent sensitivity achievable by monitoring the reflectance in case of LYZ and AuNP-LYZ seeding, we have mapped the polar and azimuthal angle dependent reflectance on the designed chip. The modification of the reflectance caused by biomolecule and bioconjugate seeding, as well as the difference between the reflectance modifications is illustrated in Fig. 4. In case of covering by either of LYZ biomolecules or AuNP-LYZ bioconjugates, both the secondary and the primary minima are modified.

The reflectance modification is enhanced in case of the secondary minimum for both bio-coverings. Moreover, comparison of reflectance differences proves that conjugation with Au NPs results in azimuthal orientation dependent sensitivity enhancement, which effect is more significant on the secondary minimum (Figs. 4(d) and 4(e)-to-4(f)). This is due to the enhanced excitation of LSPR on the AuNPs via LRSPP propagating along the valley at the secondary minimum, which is described in **Section 3.5** and in the **Appendix**.

The numerical computations on the designed chip have shown that the shift of the resonance minima caused by a specific biocovering sensitively depends on the azimuthal orientation. Namely, in $\gamma_{\text{designed_chip}} = 28^\circ$ azimuthal orientation only one single primary minimum is observable on the reflectance at $\phi_{\text{designed_chip_}\gamma=28^\circ}^{\text{primary}} = 51.8^\circ$, which is almost insensitive to the biomolecule seeding through $N_{\text{designed_chip+LYZ/AuNP-LYZ_bottom}} = 8$ number of bio-objects per unit cell, independently of the Au NPs presence (Fig. 2(d) with inset).

In $\gamma_{\text{designed_chip}} = 33.64^\circ$ azimuthal orientation the reflectance exhibits double minima with the same depth on all of the bare, LYZ and AuNP-LYZ covered designed biochips (Fig. 2(c)). On the bare designed chip the secondary minimum appears at $\phi_{\text{designed_chip_}\gamma=33.64^\circ}^{\text{secondary}} = 48.6^\circ$, which is smaller than the polar angle corresponding to the measured secondary minimum, according to the significantly smaller average PC layer thickness (Fig. 2(c)). As a result of covering by $N_{\text{designed_chip+LYS_bottom}} = 8$ protein biomolecules per unit cell at the bottom of the valley, the secondary minimum appears at $\phi_{\text{designed_chip+LYZ_bottom_}\gamma=33.64^\circ}^{\text{secondary}} = 49^\circ$, corresponding to $\Delta\phi_{\text{designed_chip+LYZ_bottom_}\gamma=33.64^\circ}^{\text{secondary}} = 0.4^\circ$ polar angle shift, which approximates the measured shift, by taking into account the accuracy of measurements.

Covering the valley by the same $N_{\text{designed_chip+AuNP-LYZ_bottom}} = 8$ number of AuNP-LYZ bioconjugates per unit cell results in a secondary minimum at $\phi_{\text{designed_chip+AuNP-Lys_bottom_}\gamma=33.64^\circ}^{\text{secondary}} = 49.4^\circ$, corresponding to a two-times larger $\Delta\phi_{\text{designed_chip+AuNP-LYZ_bottom_}\gamma=33.64^\circ}^{\text{secondary}} = 0.8^\circ$ polar angle shift, which again approximates the measured shift, by taking into account the accuracy of measurements.

Comparison of the effect of LYZ biomolecules and AuNP-LYZ bioconjugates proves that in case of the designed chip at the bottom of the valley 15-times and 2-times less amount of bioseeders results in the same shift, than in case of the fitted chip. This indicates that the interaction cross-section between the plasmonic modes that are at play is strongly enhanced already in the valley, when the minimal layer thickness is applied. Explanation of the underlying nanophotonical phenomena is presented in **Section 3.5** and in the **Appendix**.

In contrast, a primary minimum also appears at $\phi_{\text{designed_chip_}\gamma=33.64^\circ}^{\text{primary}} = 54.0^\circ$ on the designed chip, however this is backward shifted in case of covering by $N_{\text{designed_chip+LYZ/AuNP-LYZ_bottom}} = 8$ LYZ biomolecules and AuNP-LYZ bioconjugates per unit cell (Fig. 2(c)). Namely, the primary minimum appears at a polar angle of $\phi_{\text{designed_chip+LYZ_bottom_}\gamma=33.64^\circ}^{\text{primary}} = 53.8^\circ$ / $\phi_{\text{designed_chip+AuNP-LYZ_bottom_}\gamma=33.64^\circ}^{\text{primary}} = 53.6^\circ$, which corresponds to a backward shift of

$\Delta\phi_{\text{designed_chip+LYZ_bottom_}\gamma=33.64^\circ}^{\text{primary}} = -0.2^\circ$ / $\Delta\phi_{\text{designed_chip+AuNP-LYZ_bottom_}\gamma=33.64^\circ}^{\text{primary}} = -0.4^\circ$, respectively.

These results indicate that the LRSPP mode, that ensures enhanced sensitivity at the secondary minima, is not at play at the primary minima, see **Section 3.5** and the **Appendix**.

In $\gamma_{\text{designed_chip}} = 38^\circ$ azimuthal orientation again one single minimum appears on the reflectance at $\phi_{\text{designed_chip}\gamma=38^\circ}^{\text{secondary}} = 49.4^\circ$, which is a secondary minimum, while there is no primary minimum in this azimuthal orientation (Fig. 2(e) with inset).

This secondary minimum does not shift noticeably in case of covering by $N_{\text{designed_chip+LYZ_bottom}} = 8$ biomolecules per unit cell, while in presence of $N_{\text{designed_chip+AuNP-LYZ_bottom}} = 8$ bioconjugates a small $\Delta\phi_{\text{designed_chip+AuNP-LYZ_bottom_}\gamma=38^\circ}^{\text{secondary}} = 0.2^\circ$ polar angle shift is observable resulting in a minimum at $\phi_{\text{designed_chip}\gamma=38^\circ+\text{AuNP-LYZ_bottom_}\gamma=33.64^\circ}^{\text{secondary}} = 49.6^\circ$.

In case of LYZ seeding the 1214 sensitivity and 191 FOM values at the secondary minimum are commensurate with the values achieved via special e.g. via GCSPP bio-sensing methods, while the 607 sensitivity and 41 FOM values at the primary minimum are commensurate with parameters published for standard grating based bio-sensing methods [19, 22, 23]. In contrast, in case of AuNP-LYZ both the 7366 sensitivity and the 1249 FOM values at the secondary minimum are significantly larger, than the highest values published for GCSPP, while the 3683 sensitivity and the 252 FOM values at the primary minimum are in the order of magnitude of the GCSPP parameters [19]. By comparing the fitted and designed biochips the ratio of the sensitivity values is in accordance with the ratio of the number of LYZ biomolecules and AuNP-LYZ bioconjugates, while the slightly different ratio of the FOM values is caused by the modified FWHM of the reflectance minima (Table 1).

These results indicate that the course of the reflectance curve observable in case of rotated grating-coupling phenomenon as well as the sensitivity and FOM achievable by monitoring the reflectance minima strongly depends on the azimuthal orientation. An optimal azimuthal orientation exists for each bio-sensing chip, in which the largest polar angle shift is achievable. Moreover, in case of the designed chip this azimuthal orientation is also a critical one, since azimuthal angle detuning causes that one of the coupled minima disappears. In practical applications, the optimal azimuthal orientation can be determined for a specific multilayer by a feedback procedure. The achieved parameters prove that it is possible to significantly improve the sensitivity and FOM of bio-sensing via RGC-SPR phenomenon on a designed biochip.

3.5 Near-field distribution on the designed chip

Comparison of the near-field distribution uncovers the origin of different sensitivities achievable in different azimuthal orientations of the designed RGC-SPR chip.

In $\gamma_{\text{designed_chip}} = 28^\circ$ azimuthal orientation the **E**-field maximum is coincident with the hill of the polymer grating (Fig. 5(a)/a-c, right, Fig. 9(a)/a-c left and middle). The E_y component exhibits hybrid distribution horizontally as well as vertically, with a turning line at the center of the valley (Fig. 5(a)/a-c, left and middle, $x = 260$ nm and 676 nm). Moreover, the E_y component is hybrid also perpendicularly to the grating (Fig. 9(a)/a-c right). These field distributions reveal that a SRSPP exists in the valley at the primary dip in this azimuthal orientation. Both the LYZ biomolecules and the AuNP-LYZ bioconjugates are located at the **E**-field minimum in the valley, where not only the **E**-field is weak, but also the interaction length with the SRSPP is small. As a consequence, the sole primary reflectance dip is not sensitive to the LYZ biomolecules and AuNP-LYZ bioconjugates presence. Accordingly, no noticeable polar angle shift of this sole resonance dip is observable in this azimuthal orientation of the designed chip (Fig. 2(d) with inset, Fig. 5(a)/a-c, Fig. 9(a)/a-c).

At the secondary dip appearing in $\gamma_{\text{designed_chip}} = 33.64^\circ$ azimuthal orientation the area corresponding to global **E**-field maximum is coincident with the left side of the valley (Fig. 5(b)/a-c, right, Fig. 9(b)/a-c left). The E_y longitudinal component is horizontally antisymmetrical with a turning line at the right border of the valley and hill (Fig. 5(b)/a-c, left, $x = 364$ nm and 780 nm). In addition to this, the E_y longitudinal component is antisymmetrical in the vertical cross-sections taken along the valley at the turning line and throughout the unit cell except exactly at the valley center, where it is slightly hybrid (Fig. 5(b)/a-c, middle). However, the E_y longitudinal component is hybrid perpendicularly to the grating (Fig. 9(b)/a-c, right).

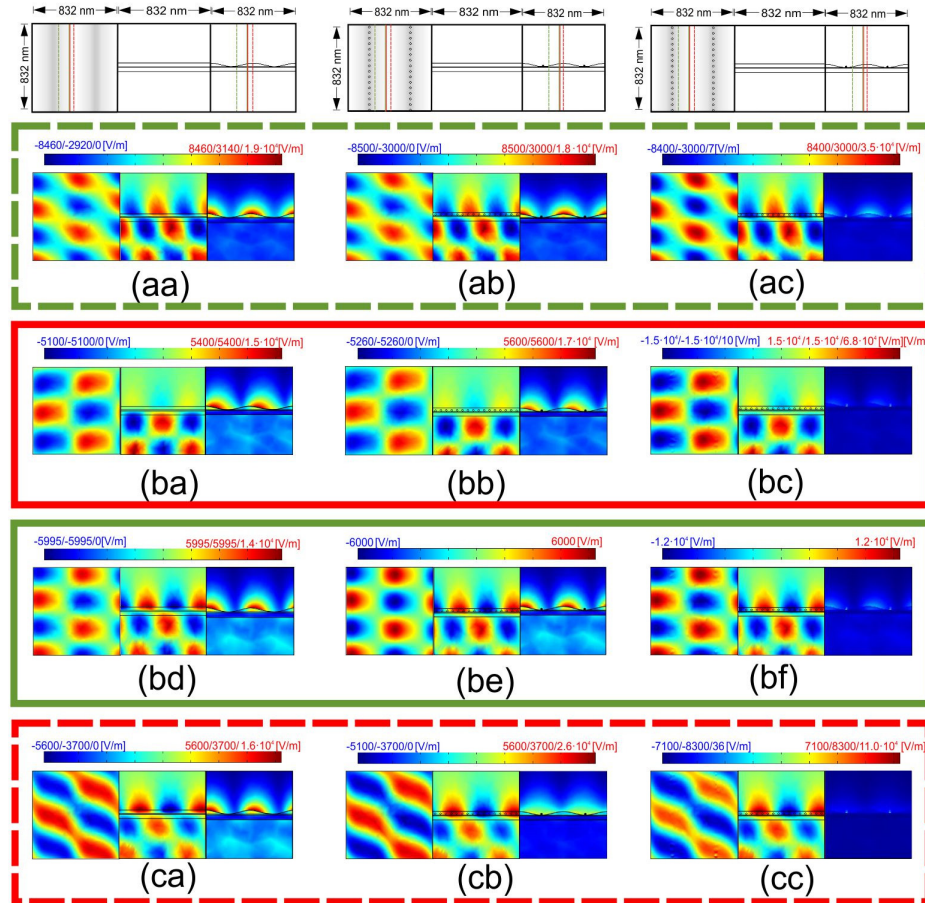


Fig. 5. The E_y field component in planes taken horizontally (x-y plane: left) and vertically along the valley at the turning line of the E_y field component (y-z plane: middle) and the normalized (**E**)-field distribution perpendicular to the unit cell (x-z plane: right), (a-c/a, b/d) on a bare designed chip, (a-c/b, b/e) on a designed chip covered by 8 LYZ biomolecules per unit cell, (a-c/c, b/f) on a designed chip covered by 8 AuNP-LYZ bioconjugates per unit cell, (a/a-c) in $\gamma_{\text{designed}} = 28^\circ$ azimuthal orientation at the primary minimum, (b/a-c and d-f) in $\gamma_{\text{designed}} = 33.64^\circ$ azimuthal orientation at the secondary and primary minimum, and (c/a-c) in $\gamma_{\text{designed}} = 38^\circ$ azimuthal orientation at the secondary minimum (see Visualization 1). The schematic drawings indicate the structure contours in different plane cross-sections and the turning lines of the E_y field component at the secondary (red) and primary (green) minima.

These near-field phenomena prove that a horizontally and vertically antisymmetric LRSPP mode propagates along the border of the valley and hill in this configuration, which ensures large interaction cross-section with the covering biolayers. The lateral extension of the E -field maximum ensures that both the LYZ biomolecules and the AuNP-LYZ bioconjugates located at the bottom of valley are inside areas shined with an intense E -field originating from the coupled LRSPP (Fig. 5(b)/b, c, right, Fig. 9(b)/b, c, left). The secondary dip in reflectance is strongly sensitive to the bio-objects presence, as a result the largest polar angle shift is observable in this azimuthal orientation (Fig. 2(c) with inset, Fig. 5(b)/a-c).

This indicates that the overlap between the bio-objects and the E -field maximum of LRSPP is sufficient, while the perfect overlap with the turning line of the E_y antisymmetry is not required to achieve significant sensitivity enhancement.

In contrast, at the primary dip appearing in $\gamma_{\text{designed_chip}} = 33.64^\circ$ azimuthal orientation smaller area corresponds to the global E -field maximum at the left side of the valley, which is shifted towards the valley with a smaller extent (Fig. 5(b)/d-f, right, Fig. 9(b)/d-f, left). The E_y component is antisymmetrical horizontally with turning line at the right edge of the valley, similarly to that at the secondary dip (Fig. 5(b)/d-f, left, $x = 364$ nm and 780 nm). In contrast, the E_y component is hybrid in the vertical cross-sections taken along the valley at the turning line and throughout the unit cell except at the valley center, where it is symmetric (Fig. 5(b)/d-f, middle). Moreover, the E_y component is hybrid perpendicularly to the grating (Fig. 9(b)/d-f, right). These near-field phenomena prove that a SRSPP mode exists in the valley at the primary minimum and is coupled with the LRSPP at the secondary minimum in this configuration. The smaller lateral extension of the E -field maximum allows smaller spatial overlap, and the SRSPP can ensure inherently smaller interaction cross-section with the LYZ biomolecules and the AuNP-LYZ bioconjugates at the bottom of the valley (Fig. 5(b)/e, f, Fig. 9(b)/e, f). As a consequence, the primary dip in reflectance is moderately sensitive to the bio-objects presence. Moreover, it exhibits a backward shift and a slight broadening caused by bio-objects adherence (Fig. 2(c) with inset, Fig. 5(b)/d-f, Fig. 9(b)/d-f). Complementary studies revealed that adherence of larger amount of bio-objects can cause disappearance of this minimum, according to the critical nature of the configuration.

Finally, in the $\gamma_{\text{designed_chip}} = 38^\circ$ azimuthal orientation the E -field maximum covers completely the left side of the valley (Fig. 5(c)/a-c, right, Fig. 9(c)/a-c, left). The E_y longitudinal component is hybrid horizontally as well as vertically in the plane cross-sections taken along the valley, at the turning line on the top of the hill and throughout the unit cell (Fig. 5(c)/a-c, left and middle, $x = 416$ nm and 832 nm). Moreover, the E_y longitudinal component is hybrid perpendicularly to the grating as well (Fig. 9(c)/a-c, right). These field distributions indicate that a SRSPP mode exists in the valley in this configuration. The location of both the LYZ biomolecules and AuNP-LYZ bioconjugates at the bottom of the valley is inside the E -field intensity maximum (Fig. 5(c)/b, c right, Fig. 9(c)/a-c, left and middle). However, the SRSPP possesses a reduced interaction cross-section with the covering biolayers caused by the inherently short propagation distance. As a consequence, the sensitivity of the secondary reflectance dip is moderate in this azimuthal orientation (Fig. 2(e) with inset).

The horizontally and vertically antisymmetric coupled LRSPP modes excited at the secondary dips in $\gamma_{\text{designed_chip}} = 33.64^\circ$ azimuthal orientation of the designed chip are unique. The E -field distribution and the large propagation distance of LRSPPs makes possible sensitivity enhancement via enhanced interaction cross-section with the LYZ biomolecules and AuNP-LYZ bioconjugates, even if they are located at the bottom of the valley, not exactly at the turning line of the antisymmetric E_y at the border of the valley and hill. The horizontally and vertically antisymmetric LRSPPs are secondary modes, which originate from the intense laterally Bragg scattered SPPs, accordingly their wave vector is smaller than that of the original SPP modes [16].

Comparison of the \mathbf{E} -field and E_y distributions proves that the vertical plane cross-section along the right border of the valley and hill, which is opposite to the side of illumination, can be considered as the metal-dielectric interface of their propagation. The horizontal and vertical antisymmetry of the E_y component ensures the minimal attenuation of these modes. The coupled LRSPs possess both larger wavelength and larger propagation length (Fig. 5(b)/a-c, Fig. 9(b)/a-c). The horizontal antisymmetry holds also for the modes coupled at the primary dips, however these modes are accompanied by hybrid E_y distribution in the vertical plane cross-section at the turning line, as a consequence they suffer larger attenuation.

The resonant excitation of AuNPs in the bioconjugates is promoted both at $\gamma_{\text{designed_chip}} = 33.64^\circ$ and $\gamma_{\text{designed_chip}} = 38^\circ$ azimuthal angles, which results in further enhanced sensitivity. Although, the local \mathbf{E} -field enhancement is the largest in $\gamma_{\text{designed_chip}} = 38^\circ$ azimuthal orientation, i.e. when the global \mathbf{E} -field maximum overlaps better with the AuNPs, the SRSP suffers larger attenuation in the valley.

As a consequence, larger sensitivity enhancement was achieved via the secondary dip in $\gamma_{\text{designed_chip}} = 33.64^\circ$ azimuthal orientation, due to the enhanced interaction cross-section with the unique LRSP (Visualization 1 corresponding to Fig. 5 about the E_y field distribution at the secondary and primary dips in different azimuthal orientations is provided in a Supplementary Material).

3.6 Dispersion characteristics of the modes accompanying RGC-SPR

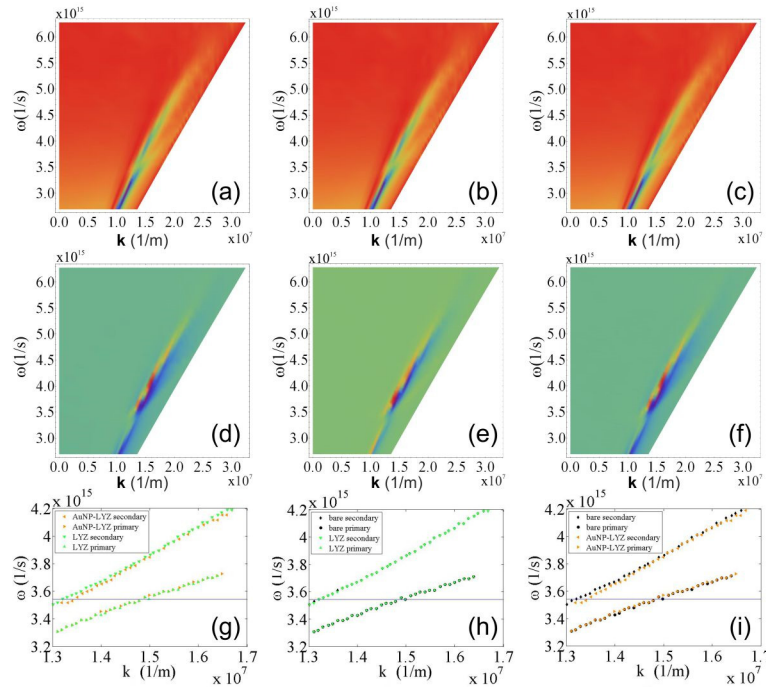


Fig. 6. Dispersion characteristics in reflectance of (a) a bare designed chip, (b) a designed chip covered by 8 LYZ biomolecules per unit cell, (c) a designed chip covered by 8 AuNP-LYZ bioconjugates per unit cell, in $\gamma_{\text{designed}} = 33.64^\circ$ azimuthal orientation. (d) Difference between reflectance modifications, (e, f) modifications of reflectance on a designed chip caused by seeding with (e) 8 LYZ biomolecules per unit cell and (f) 8 AuNP-LYZ bioconjugates per unit cell compared to the bare designed chip. Comparison of locations corresponding to secondary and primary minima (g) 8 AuNP-LYZ to LYZ covering, (h/i) 8 LYZ / 8 AuNP-LYZ covered chip to bare designed chip.

The dispersion characteristics of the designed chip was mapped in $\gamma_{\text{designed_chip}} = 33.64^\circ$ azimuthal orientation and shows that two anti-crossing plasmonic bands coexist (Fig. 6). The lower band is similar to the usual unperturbed plasmonic band on a flat dielectric-metal interface, however, it is deformed caused by the splitting originating from rotated grating-coupling. The hybridized modes exhibit a well-defined turning line in their horizontally antisymmetric E_y component, which is in accordance with the phase map formed during Bragg scattering in the optimal azimuthal orientation (Fig. 5(b)/a-c, left).

However, they are antisymmetrical and hybrid in the vertical plane cross-section taken at the turning line of the horizontally antisymmetric E_y field component along the border of the valley and hill for the secondary and primary minimum, respectively (Fig. 5(b)/ a-c and Fig. 5(b)/d-f, middle). On the designed chip at the secondary reflectance minimum a unique rotated grating-coupled LRSPP exists due to the co-existent horizontal and vertical antisymmetry. This LRSPP is strongly coupled with the SRSPP mode at the primary minimum.

The rotated grating coupling results in a PBG at the boundary of the first Brillouin zone, and the azimuthal orientation dependent wave vector corresponding to the gap center position can be computed as: $k_{\parallel} = \pi/p \cdot \cos \gamma$, in accordance with the literature [7]. The differences in the achieved reflectance (Fig. 6(d)-6(f)) and the locations of the reflectance minima unambiguously show that the secondary minimum exhibits a significantly larger shift throughout a wide spectral interval. The largest shift is achievable at ~ 532 nm for the designed biochip, and the Au NPs enhance the polar angle shift of the resonance minima (Fig. 6(g)-6(i)).

4. Conclusion

SPR measurements were performed and numerical computations were realized to analyze the effect of seeding by LYZ biomolecules and AuNP-LYZ bioconjugates on the reflectance minima originating from rotated grating-coupling on wavelength-scaled polymer gratings. The SPR measurements performed in conical mounting proved that the monitoring of the secondary minima in the optimal azimuthal orientation is more suitable to detect adhered bio-objects, than the observation of the broader primary minima. These results were proven via FEM computations on a fitted and on a designed biochip as well.

Numerical computations on the fitted chip revealed that the measured secondary minimum shifts can be reproduced by positioning large number of LYZ biomolecules and significantly smaller number of AuNP-LYZ bioconjugates at the bottom of the valley. Comparative studies on the effect of specific bio-objects prove that the secondary minimum is more strongly shifted than the primary one, moreover the primary minimum exhibits a broadening. The sensitivity can be improved by ensuring that the location of biomolecules approaches the turning line of the E_y field component at the right border of the valley and hill, where the horizontally and vertically antisymmetric coupled LRSSP propagates. The optimal location ensures overlap with the local \mathbf{E} -field maximum on the right side of the valley as well, which corresponds to the coupled LRSPP. The enhanced sensitivity of the secondary resonance minima is the result of the large interaction cross-section achievable via LRSPPs. Moreover the secondary minimum exhibits larger concentration sensitivity as well.

The near-field study performed on the designed chip demonstrated that the \mathbf{E} -field is confined onto the hill / at the border of the hill and valley / onto the left side of the valley of the polymer grating, when no primary minimum shift / maximal secondary minimum shift / moderate secondary reflectance minimum shift is observable in 28° / 33.64° / 38° azimuthal orientation. These \mathbf{E} -field distributions are accompanied by E_y field-component distribution, which is hybrid / antisymmetrical vertically as well as horizontally with respect to the turning line / hybrid.

The field distribution proves that short-range / horizontally and vertically antisymmetric long-range / short-range mode exists in these configurations in the valley of the designed chip, where the bio-objects are adhered.

It was also demonstrated that the **E**-field confinement promotes excitation of LSPR on the Au NPs in bio-conjugates. As a result, the Au NPs enhance the difference between the polar angles corresponding to reflectance minima on bare and LYZ covered chips, which reveals that noble metal particles can be used to enhance the biodetection sensitivity significantly. The sensitivity and FOM values are the largest for the secondary minimum observable in the optimal azimuthal orientation of the designed RGC-SPR chip.

In conclusion, considerable sensitivity enhancement is achievable in the optimal RGC-SPR configuration of the designed chip due to the LRSP originating from SPP Bragg scattering, and the sensitivity is significantly enhanced, when bioconjugates are detected. Each bio-sensing multilayer consisting of a wavelength-scaled grating has its own optimal configuration, which corresponds to the optimal azimuthal orientation, capable of resulting in the largest polar angle shift. In the optimal configuration, the coupling efficiency of the horizontally and vertically antisymmetric LRSP, as well as the spatial overlap between the bio-objects and the LRSP is maximized.

Appendix

In case of seeding by LYZ biomolecules the FOM of the secondary minimum is larger than the FOM of the primary minimum for both locations at the bottom of the valley and on the hillside, throughout the complete inspected concentration interval. The FOM of the secondary (primary) minimum is larger (smaller) on the hillside than at the bottom of the valley, throughout the complete inspected concentration interval.

In case of seeding by AuNP-LYZ bioconjugates the FOM of the secondary minimum is larger than the FOM of the primary minimum for both locations at the bottom of the valley and on the hillside, throughout the complete inspected concentration interval. Moreover, there is a FOM maximum for the secondary minimum at the inspected 16 NPs/unit cell. The FOM of the secondary (primary) minimum is larger (smaller) on the hillside than at the bottom of the valley, throughout the complete concentration interval (when the concentration is smaller than 24 AuNP-LYZ/unit cell).

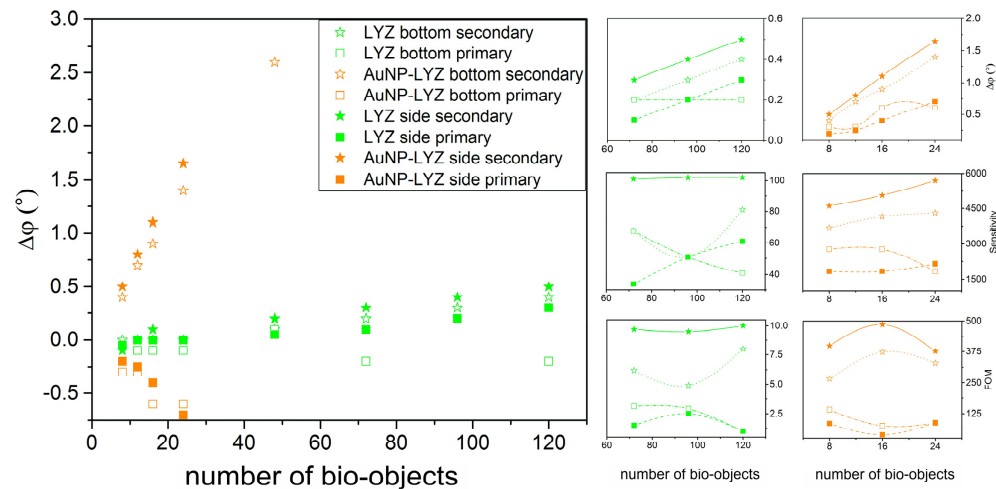


Fig. 7. Concentration dependence of the polar angle shift in case of different bio-objects and locations. Insets: absolute value of the polar angle shift (top), sensitivity (middle) and FOM (bottom) for concentrations surrounding the 120 LYZ/unit cell (left) and 16 AuNP-LYZ/unit cell (right) on the fitted chip.

Table 1. Secondary and primary minima on the measured and computed reflectance curves, the corresponding polar angle shifts ($\Delta\phi$), surface angular sensitivity (S_ϕ) and FOM values*.

		$\phi^{\text{sec}}(^{\circ})$	$\phi_{\text{LYZ}}^{\text{sec}}(^{\circ})$		$\phi_{\text{AuNP-LYZ}}^{\text{sec}}(^{\circ})$		$\phi^{\text{pri}}(^{\circ})$	$\phi_{\text{LYZ}}^{\text{pri}}(^{\circ})$		$\phi_{\text{AuNP-LYZ}}^{\text{pri}}(^{\circ})$	
			$\Delta\phi_{\text{LYZ}}^{\text{sec}}(^{\circ})$		$\Delta\phi_{\text{AuNP-LYZ}}^{\text{sec}}(^{\circ})$			$\Delta\phi_{\text{LYZ}}^{\text{pri}}(^{\circ})$		$\Delta\phi_{\text{AuNP-LYZ}}^{\text{pri}}(^{\circ})$	
			S_{ϕ}	FO M	S_{ϕ}	FO M		S_{ϕ}	FO M	S_{ϕ}	FOM
Measured $\gamma \sim 30^{\circ}$		52.16	52.48				64.96	64.2			
			0.32					-0.76			
			65	8				156	2		
		50.72			51.6		69.44			64.64	
					0.88					-4.8	
				4054	459				22113	947	
Fitted bottom $\gamma = 29.5^{\circ}$	$N_b = 0$	53.4					72.6				
	$N_b = 120$		53.8					72.4			
			0.4					-0.2			
			81	8				41	1.4		
	$N_b = 16$				54.3					72.0	
					0.9					-0.6	
				4146	373				2764	76	
Fitted hillside $\gamma = 29.5^{\circ}$	$N_s = 0$	53.4					72.6				
	$N_s = 120$		53.9					72.9			
			0.5					0.3			
			102	10				61	1.2		
	$N_s = 16$				54.5					72.2	
					1.1					-0.4	
				5067	486				1843	39	
Designed $\gamma = 33.64^{\circ}$	$N_b = 0$	48.6					54.0				
	$N_b = 8$		49.0					53.8			
			0.4					-0.2			
			1214	191				607	41		
	$N_b = 8$				49.4					53.6	
					0.8					-0.4	
				7366	1249				3683	252	
Designed $\gamma = 38^{\circ}/28^{\circ}$	$N_b = 0$	49.4					51.8				
	$N_b = 8$		49.4					51.8			
			0.0					0.0			
			0	0				0	0		
	$N_b = 8$				49.6					51.8	
					0.2					0.0	
				1841	511				0	0	

*The effective index of refraction corresponding to a thin layer of LYZ [22, 23]:

$$n_{\text{eff}} = n_{\text{LYZ}} + (n_{\text{air}} - n_{\text{LYZ}}) \cdot \exp\left(-\frac{2 \cdot d_{\text{LYZ}}}{L_{\text{decay}}^{\text{air}}}\right), \text{ where } n_{\text{LYZ}} \text{ and } n_{\text{air}} \text{ is the index of refraction of LYZ and air, } d_{\text{LYZ}}$$

is the LYZ layer thickness, and $L_{\text{decay}}^{\text{air}}$ is the decay length at the multilayer and air interface. The S_ϕ surface angular sensitivity was computed by taking into account the modification of the effective index of refraction:

$$S_\phi = \Delta\phi / \left[(n_{\text{air}} - n_{\text{LYZ}}) \cdot \left(1 - \exp\left(-\frac{2 \cdot d_{\text{LYZ}}}{L_{\text{decay}}^{\text{air}}}\right) \right) \right].$$

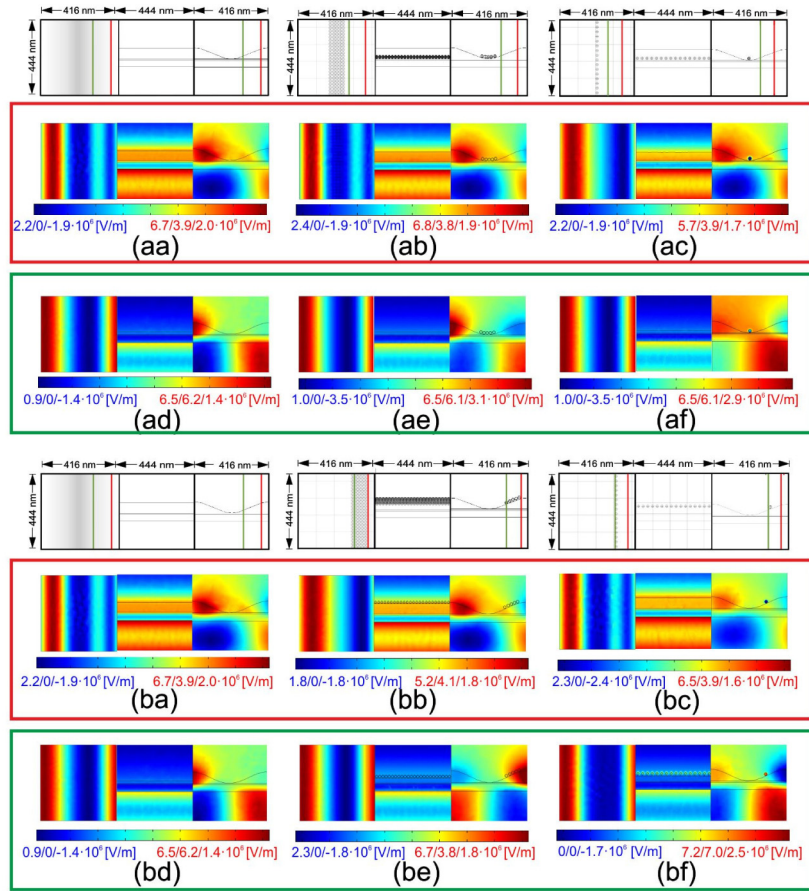


Fig. 8. The normalized (E)-field distribution in planes taken horizontally (x - y plane: left) and vertically along the valley at the turning line of E_y (y - z plane: middle) and the E_y field component distribution perpendicularly to the unit cell (x - z plane: right) on (a,b/ a,d) bare fitted chip, (a,b/ b,e) fitted chip covered by LYZ biomolecules, (a,b/ c,f) fitted chip covered by AuNP-LYZ bioconjugates, in 29.5° azimuthal orientation of the fitted chip (a,b/ a-c) secondary and (a,b/ d-f) primary minima in case of bio-objects at the (a/ a-f) bottom of valley and (b/ a-f) side of the hill. The schematic drawings indicate the structure contours in different plane cross-sections and the turning lines of the E_y field component at the secondary (red) and primary (green) minima.

Both on the fitted and on the designed chip, in absence and presence of bio-object coverings, at all secondary dips arising on split reflectance curves exhibiting two minima, the E -field enhancement in the vertical cross-section taken along the valley below the metal layer proves the co-existence of a glass side plasmon (Figs. 8(a) and 8(b)/a, b, c middle, Fig. 9(b)/a, b, c middle).

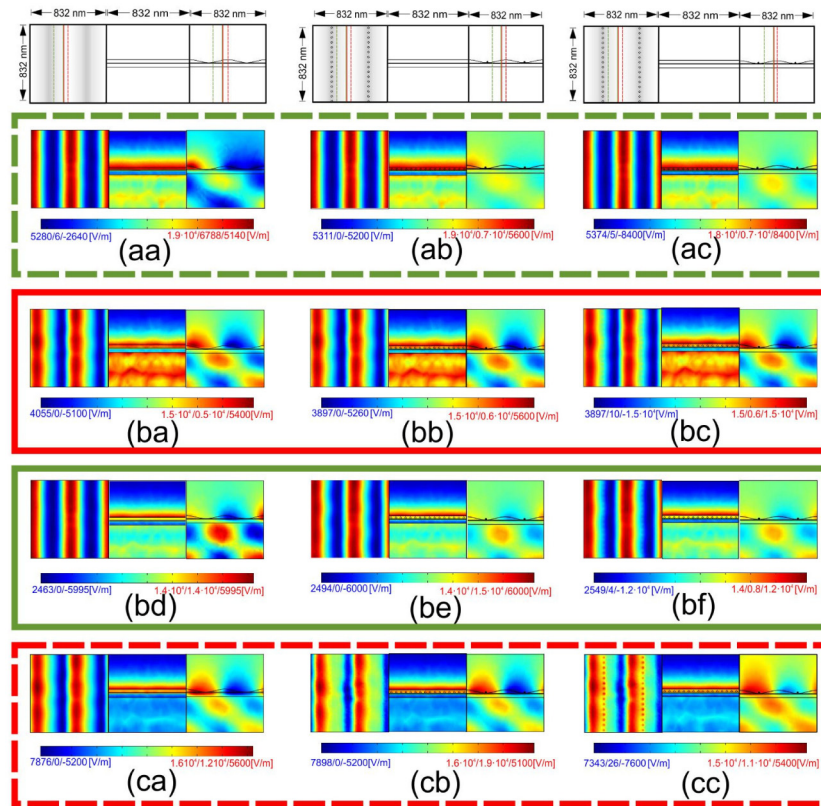


Fig. 9. The normalized E-field distribution in planes taken horizontally (x-y plane: left) and vertically along the valley at the turning line of the E_y field component (y-z plane: middle) and the E_y field component distribution perpendicularly to the unit cell (x-z plane: right), (a-c/a, b/d) on a bare designed chip, (a-c/b, b/e) on a designed chip covered by 8 LYZ biomolecules per unit cell, (a-c/c, b/f) on a designed chip covered by 8 AuNP-LYZ bioconjugates per unit cell, (a/a-c) in $\gamma_{\text{designed}} = 28^\circ$ azimuthal orientation at the primary minimum, (b/a-c and d-f) in $\gamma_{\text{designed}} = 33.64^\circ$ azimuthal orientation at the secondary and primary minimum, and (c/a-c) in $\gamma_{\text{designed}} = 38^\circ$ azimuthal orientation at the secondary minimum. The schematic drawings indicate the structure contours in different plane cross-sections and the turning lines of the E_y field component at the secondary (red) and primary (green) minima.

Funding

National Research, Development and Innovation Office-NKFIH (K116362, K116323 and GINOP-2.3.2-15-2016-00013); Hungarian Academy of Sciences.

Acknowledgement

The research was supported by National Research, Development and Innovation Office-NKFIH through project “Optimized nanoplasmonics” K116362; “Synthesis, structural and thermodynamic characterization of nanohybrid systems at solid-liquid interfaces” K116323 and GINOP-2.3.2-15-2016-00013. Mária Csete and Edit Csapó acknowledge that the project was supported by the János Bolyai Research Scholarship of the Hungarian Academy of Sciences.

The authors would like to thank András Szenes, Hajnalka Milinszki and Lóránt Szabó for figures preparation.